Proposal for a Hydrogen Bond Network in the Active Site of the Prototypic γ-Class Carbonic Anhydrase†

Sabrina A. Zimmerman and James G. Ferry*

Department of Biochemistry and Molecular Biology, Eberly College of Science, The Pennsylvania State University, University Park, Pennsylvania 16802-4500

Received December 8, 2005; Revised Manuscript Received March 5, 2006

ABSTRACT: The crystal structure of Cam, the prototypic γ-class carbonic anhydrase, reveals active site residues Gln75, Asn73, and Asn 202 previously hypothesized to participate in catalysis. These potential roles were investigated for the first time by kinetic analyses of site-specific replacement variants of the zinc and cobalt forms of Cam. Gln75 replacement variants showed large decreases in k_{cat}/K_m relative to wild-type. Further, the Gln75 variants showed a loss of the pK_a in pH versus k_{cat}/K_m profiles previously attributed to ionization of the metal-bound water yielding the hydroxyl group attacking CO_2. These results support the previously proposed role for Gln75 in hydrogen bonding with the catalytic hydroxyl orienting it for attack on CO_2. Kinetic analyses of Asn73 variants were consistent with a role in hydrogen bonding with Gln75 to position it for optimal interaction with the catalytic hydroxyl. Kinetic analyses of Asn202 variants showed substantial decreases in k_{cat}/K_m relative to the wild-type enzyme supporting the previously hypothesized role in polarizing CO_2 and facilitating attack from the metal-bound hydroxyl. On the basis of results presented here, and previously reported structural analyses, we present a catalytic mechanism involving Gln75, Asn73, and Asn202 that also suggests a role for Glu62 not previously recognized. Finally, the results suggest that the γ-, β-, and α-class carbonic anhydrases each independently evolved variations of a fundamental hydrogen bond network essential for catalysis.

Carbonic anhydrases (CAs)[1] are metalloenzymes that catalyze the reversible hydration of carbon dioxide to bicarbonate (eq 1) (*1*). To date, there are six classes of

$$CO_2 + H_2O \rightleftarrows HCO_3^- + H^+ \quad (1)$$

independently evolved CAs that have no significant sequence identity (*2*−*6*). Mounting kinetic evidence for three (α, β, and γ) of the six classes of CAs indicate a two-step isomechanism for the interconversion of carbon dioxide and bicarbonate (eqs 2a,b and 3a,b) (*7*−*18*). In the equations, E refers to enzyme, M refers to the metal, and B refers to a buffer molecule. The CO_2 hydration step (eqs 2a and 2b) is

$$E-M^{2+}-OH^- + CO_2 \rightleftarrows E-M^{2+}-HCO_3^- \quad (2a)$$

$$E-M^{2+}-HCO_3^- + H_2O \rightleftarrows E-M^{2+}-H_2O + HCO_3^- \quad (2b)$$

$$E-M^{2+}-H_2O \rightleftarrows H^+-E-M^{2+}-OH^- \quad (3a)$$

$$H^+-E-M^{2+}-OH^- + B \rightleftarrows E-M^{2+}-OH^- + BH^+ \quad (3b)$$

reflected by k_{cat}/K_m. During this first step, the lone pair of electrons of the metal-bound hydroxide nucleophilically attack the incoming CO_2 molecule (eq 2a). The resulting bound HCO_3^- undergoes a continuum of binding motifs, ultimately being displaced by an incoming water molecule (eq 2b). The second step, proton transfer, refers to the regeneration of the catalytic metal-bound hydroxide by extracting a proton from the metal-bound water (eq 3a) and transfer out to buffer (eq 3b) (*19*). Proton transfer, when rate-limiting, is reflected by k_{cat}. CAs with k_{cat} greater than 10^4 s^{-1} employ active site residue(s) that shuttle the proton to buffer (*20*).

Rigorous exploration of the well-characterized α-class CA, HCAII, has identified two residues essential for the CO_2 hydration step, Thr199 and Glu106 (*11*, *13*, *21*−*23*). The Thr199 hydroxyl hydrogen-bonds with the carboxylate oxygen of Glu106. This interaction orients the Thr199 hydroxyl to act as a hydrogen bond acceptor to the zinc-bound hydroxide, optimizing orientation of the lone pair of electrons of the hydroxide for nucleophilic attack on CO_2. The backbone amide of Thr199 hydrogen bonds with the CO_2 molecule, polarizing it for nucleophilic attack and providing an environment that increases the K_d of HCO_3^- to promote product removal (*11*). Comparisons of the active sites in the crystal structures of α, β, and γ-class CAs do not reveal threonines or glutamates that correspond to α-class residues, Thr199 and Glu106. This raises the question whether active site residues exist in β- and γ-class CAs that provide the same catalytic function as those α-class residues, therefore, identifying a conserved mechanism among CAs.

Superimposition of the active site of β-class CAs from *Arabidopsis thaliana* and *Pisium sativum* on the active site

† This work was funded by a grant from the NASA Astrobiology Institute and Department of Energy Grant DE-FG02-95ER20198 to J.G.F. S.A.Z. was funded by an Alfred P. Sloan NACME Fellowship.

* Corresponding author. E-mail, jgf3@psu.edu; phone, (814) 863-5721; fax, (814) 863-6217.

[1] Abbreviations: CA(s), carbonic anhydrase(s); E, enzyme; M, metal; B, buffer.

10.1021/bi052507y CCC: $33.50
Published on Web 04/05/2006

of HCAII (*9*, *14*, *15*) revealed that *A. thaliana* active site residue, Gln158, and equivalent Gln151 in *P. sativum*, were optimally positioned to provide the same catalytic function as the backbone amide of Thr199 in HCAII (*15*). Kinetic studies of the N158A variant (*15*) support this hypothesis. The prototype of the γ-class, Cam (*24*), was first isolated from *Methanosarcina thermophila*, a methanogenic microbe from the Archaea domain (*25*). Previous inspection of the crystal structures of the wild-type Co−Cam and Zn−Cam (*8*) identified four residues adjacent to the metal in the active site that may perform conserved key roles in catalysis analogous to the α-class HCAII and β-class CAs from *A. thaliana* and *P. sativum*. The carbonyl group of Cam active site residue Gln75 is shown within hydrogen bonding distance to the metal-bound hydroxide and, when complexed with HCO_3^-, the metal-bound oxygen of HCO_3^- (*8*). This suggests Gln75 could orient and stabilize the metal-bound hydroxide. However, crystal structures also show Glu62 within hydrogen bond distance to a nonmetal oxygen of HCO_3^-; yet in uncomplexed structures, Glu62 orients toward Glu84 which acts as the primary proton shuttling residue (*8*, *26*). Though kinetic analyses of Glu62 variants (*26*) indicate participation in CO_2 hydration, the specific function is unknown, and a role in proton transfer could not be ruled out. Glu62 is unlikely to act as the primary residue orienting the metal-bound hydroxide, since Glu62 is not conserved among the putative γ-class CAs; however, Gln75 is strictly conserved. This leads to the proposal that Gln75 and Asn73 act in a hydrogen bond network with the metal-bound hydroxide analogous to the Zn−hydroxide−Thr199−Glu106 hydrogen bond network characterized in α-class CA, HCAII (*8*, *27*). Cam crystal structures also show Asn202 within hydrogen bonding distance to a nonmetal-bound oxygen of the HCO_3^- molecule, implying a function corresponding to the backbone amide of the α-class Thr199 and β-class Gln151 in *P. sativum* and Gln158 in *A. thaliana*. Here, we present kinetic analyses of site-specific replacement variants of Cam which show Gln75 and Asn202 are essential in catalysis, whereas Asn73 has a minor role. The results suggest roles for these residues analogous to active site residues in the independently evolved α- and β-classes. Further, a more defined role for Glu62 in Cam is proposed.

EXPERIMENTAL PROCEDURES

Mutagenesis and Expression. Plasmid pBA1416NB, derived from plasmid pT7-7, encoding the sequence of Cam minus the 34-amino acid N-terminal secretory signal peptide, was used as the starting plasmid for all site-directed mutagenesis experiments (*28*). Mutations were introduced at positions encoding for amino acid residues 73, 75, and 202 using the site-directed mutagenesis kit, QuickChange by Stratagene (La Jolla, CA). Mutations were confirmed by DNA sequencing of the plasmids. *Escherichia coli* strain BL21 (DE3) was transformed with the Cam variant plasmids which were then used to inoculate Luria-Bertani broth containing 100 μg/mL ampicillin. Cells were grown at 37 °C to an A_{600} of 0.6−0.8 and induced to overproduce Cam variants with the addition of 500 μM $ZnSO_4$ and isopropyl thiogalactopyranoside (IPTG) to a final concentration of 0.8 mM, followed by continued growth at 37 °C for 4 h. Cells were harvested by centrifugation and stored frozen at −80 °C until lysis.

Purification and Reconstitution. Frozen cells were thawed and resuspended in 50 mM MOPS (pH 7.5) buffer followed by two passes through a chilled French press at a pressure of 1000 lb/in.^{2} (1 lb/in.^{2} = 6.9 kPa). The cell lysate was centrifuged at 29 000*g* for 45 min, followed by filtration of the supernatant through a 0.45 μm filter. This filtrate solution was then loaded onto a Q-Sepharose Fast Flow column (Amersham Pharmacia Biotech, Piscataway, NJ) and washed with several column volumes of 50 mM MOPS (pH 7.5) buffer. A gradient elution of 0−1.0 M NaCl was then applied over 6 column volumes. Cam variants typically eluted between 0.35 and 0.45 M NaCl. These fractions were pooled and diluted 2-fold with 3.0 M $(NH_4)_2SO_4$ in 50 mM MOPS (pH 7.5) buffer to give a final $(NH_4)_2SO_4$ concentration of 1.5 M. This solution was loaded onto a Phenyl Sepharose high-performance column (Amersham Pharmacia Biotech, Piscataway, NJ) previously equilibrated with 1.5 M $(NH_4)_2SO_4$ in 50 mM MOPS (pH 7.5) buffer. The column was washed with several bed volumes of equilibration buffer. When a decreasing salt gradient of 1.5−0 M $(NH_4)_2SO_4$ buffer was used, the Cam was eluted. Cam fractions were then pooled and desalted using a PD-10 desalting column (Amersham Pharmacia Biotech, Piscataway, NJ). Wild-type Cam and Cam variants were denatured, and then refolded in a series of metal-free 150 mM KCL in 50 mM MOPS (pH 7.5) buffer exchanges. The refolded apo-enzyme was then reconstituted with either a cobalt or zinc ion, exclusively (*7*).

Gel Filtration Chromatography. A Superdex 75 high-resolution gel filtration column (Amersham Pharmacia Biotech, Piscataway, NJ) was equilibrated with 150 mM KCl in 50 mM MOPS (pH 7.5) buffer. Each metal-reconstituted Cam variant was loaded onto the size-exclusion column and eluted using a flow rate of 1.0 mL/min. The eluting holoenzyme was detected by measuring the UV absorbance at a wavelength of 280 nm. The trimeric Cam fractions were pooled, concentrated, frozen in liquid nitrogen, and stored at −80 °C. ICP analysis was conducted on all Cam variants to determine metal content (The Chemical Analysis Laboratory, University of Georgia, Athens, GA).

Steady-State Kinetic Measurements. Wild-type Cam and Cam variants were assayed in the direction of CO_2 hydration by stopped-flow spectroscopy (*29*), using a model SF-2001 KinTek stopped-flow instrument (KinTek Corp., Austin, TX). Assays were performed at 25 °C in 50 mM HEPES (pH 7.5). The Cam variants protein concentrations were determined by first measuring the A_{280} of these protein solutions, and then using a theoretical extinction coefficient of 15 990 M^{-1} cm^{-1} with a computed monomer molecular mass of 22 873 Da. The protein concentrations for wild-type and variants are given based on the extinction coefficient of the Cam monomer. Enzyme monomer concentrations ranged from 400 nM to 6 μM. Buffer−indicator dye pairs used were MES and chlorophenol red (at pH 5.7−6.9) measured at a wavelength of 574 nm, MOPS and 4-nitrophenol (at pH 6.5−7.7) measured at a wavelength of 400 nm, and TAPS and *m*-cresol purple (at pH 7.7−9.1) measured at a wavelength of 578 nm. Buffer concentrations were all 50 mM, the total ionic strength was adjusted to 50 mM with Na_2SO_4, and final pH indicator concentrations were 50 μM. Saturated solutions of CO_2 (32.9 mM in H_2O) were prepared by bubbling CO_2 gas into deionized water at 25 °C. The experimental final

CO_2 concentrations were varied from 4.7 to 24 mM. The initial 5−10% of the total absorbance changes were used to calculate initial steady-state kinetic data used for kinetic analysis, using the average of 10−15 reaction traces per experiment. The initial rate data were fit to the Michaelis−Menten equation to obtain experimental values for k_{cat} and K_m. The pH-independent values of k_{cat} and pK_a for the CO_2 hydration reaction were determined by fitting the experimental pH-dependent Michaelis−Menten parameter k_{cat} to eq 4. The pH-independent values for k_{cat}/K_m and pK_a of the Gln75 variants were also fit to eq 4.

$$k_{cat}^{obs} = k_{cat}/(1 + 10^{(pK_a - pH)}) \quad (4)$$

The k_{cat}/K_m of wild-type Cam depends on two pK_a values (*7*); thus, the pH-independent values for k_{cat}/K_m and pK_a for the CO_2 hydration reaction of the Cam variants were determined by fitting the pH-dependent Michaelis−Menten parameter k_{cat}/K_m to eq 5.

$$k_{cat}/K_m^{obs} = (k_{cat}/K_m \times 10^{(pK_a^{II} - pH)} + k_{cat}/K_m^{II})/ (1 + 10^{(pK_a^{II} + pK_a^{I} - 2pH)} + 10^{(pK_a^{I} - pH)} + 10^{(pK_a^{II} - pH)}) \quad (5)$$

All fits described were done using Kaleidagraph (Synergy Software, Reading, PA). All effective kinetic parameters were based on protein concentrations of the monomer associated with an active site metal determined from the metal incorporation of each variant by ICP analysis.

UV/Visible Absorption Spectroscopy. Optical absorption spectra were obtained for wild-type Zn−Cam and Co−Cam as well as all generated variants at 25 °C using a Beckman DU640 spectrophotometer (Beckman Instruments, Inc., Fullerton, CA). All samples were desalted with a PD-10 desalting column (Amersham Pharmacia Biotech, Piscataway, NJ) and placed in 20 mM MOPS buffer (pH 7.0). All samples were assayed at a protein concentration of 1.1 mM. Difference spectra of wild-type and variant proteins were generated by subtracting the absorbance spectra of the Zn−Cam and Zn−Cam variants from the absorbance spectra of the respective cobalt-substituted protein.

RESULTS

Initial Characterization of Cam Variants. Crystal structures of wild-type Cam complexed with bicarbonate (*8*) identified active site residues, Gln75, Asn73, and Asn202, (Figure 1), with potential functions corresponding to residues Thr199 and Glu106 in the well-characterized α-class CAs (*11*, *13*, *27*, *30*, *31*). Thus, Cam variants, in which Gln75, Asn73, or Asn202 were individually replaced, were generated to investigate the role of these residues in catalysis (Tables 1, 3, and 4). All 13 variants were expressed in soluble form in *E. coli*, with final yields of 20−50 mg of the purified variant/L of cell culture, similar to the ∼50 mg yield of the wild-type protein. Each variant was reconstituted with cobalt or zinc with less than 1% loss of protein yield. Every reconstituted variant eluted as a single symmetrical peak from a Superdex 75 size-exclusion column corresponding to a native molecular mass of approximately 70 kDa, identical to the trimeric wild-type. The metal content determined for each variant (Tables 1, 3, and 4) was at least 0.7 metal/monomer, indicative of robust reconstitution. These results suggest that the functional integrity of each variant was similar to wild-type.

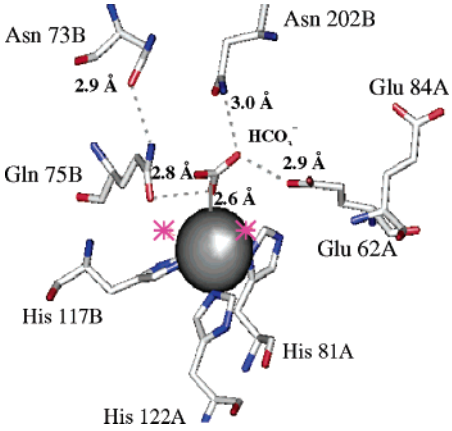

FIGURE 1: Co-Cam active site complexed with HCO_3^-. The figure was displayed with Open-Source Pymol version 0.97 2004. Letters "A" and "B" designate residues contributed by adjacent monomers. The dashed lines represent possible hydrogen bond interactions. Glu84, the proton shuttle residue, is shown in the "out" position. The two asterisks on either side of the metal represent the two metal-bound waters.

Table 1: Michaelis-Menten Steady-State Kinetic Parameters for Wild-Type Cam and Variants with Substitutions at Gln75

variant	K_m (mM)	k_{cat}^{eff} (ms^{-1})[a]	k_{cat}/K_m^{eff} ($\mu M^{-1}\ s^{-1}$)[a]	molar ratio of metal/monomer
wild-type Zn−Cam	15.6 ± 0.79	70.2 ± 7.8	4.35 ± 0.49	1.2
wild-type Co−Cam	15.3 ± 0.9	173.0 ± 4.5	11.7 ± 0.5	0.7
Zn−Q75A	26.7 ± 6.7	1.35 ± 0.21	0.051 ± 0.021	1.2
Co−Q75A	12.0 ± 1.9	0.71 ± 0.050	0.059 ± 0.013	0.7
Zn−Q75N	63.9 ± 18.2	8.29 ± 1.80	0.13 ± 0.066	1.0
Co−Q75N	72 ± 13	4.77 ± 0.07	0.07 ± 0.02	1.1
Zn−Q75D	36.4 ± 9.8	0.95 ± 0.18	0.026 ± 0.012	1.0
Co−Q75D	15.6 ± 4.1	0.75 ± 0.10	0.048 ± 0.019	0.8
Zn−Q75E	21.6 ± 6.1	0.602 ± 0.10	0.028 ± 0.012	0.8
Co−Q75E	13 ± 2.7	0.57 ± 0.051	0.044 ± 0.013	0.8

[a] Effective k_{cat} and k_{cat}/K_m values were based on the concentration of monomer associated with an active site metal determined from the molar ratio of metal/monomer.

Benefiting from its overall $3d^7$ electronic configuration, cobalt was used as a reporter metal to investigate the integrity of the active site in the variants via electronic spectroscopy since zinc does not significantly absorb in the UV/vis range. Intensity and position of the absorbance bands are dependent on the number and type of ligands coordinating the metal as well as the geometry of cobalt in the active site (*24*). The visible difference spectra of wild-type Co−Cam *minus* Zn−Cam, and alanine variants, are shown in Figure 3. The difference spectrum of wild-type had a low molar absorptivity ($\epsilon_{515\ nm} = 30\ M^{-1}\ cm^{-1}$) indicative of a hexacoordinate metal center determined empirically with cobalt standards and consistent with the previously reported structure of Co−Cam (*8*, *24*, *28*). The position of the maximum absorbance band (515 nm) corresponded to an average ligand field of three oxygens, possibly donated by water molecules, and three nitrogens that can be contributed by histidines ligating the metal, consistent with the crystal structure of Cam (*8*, *24*). The representative difference spectra of variants Co−Q75A, Co−N73A, and Co−N202A were comparable to that

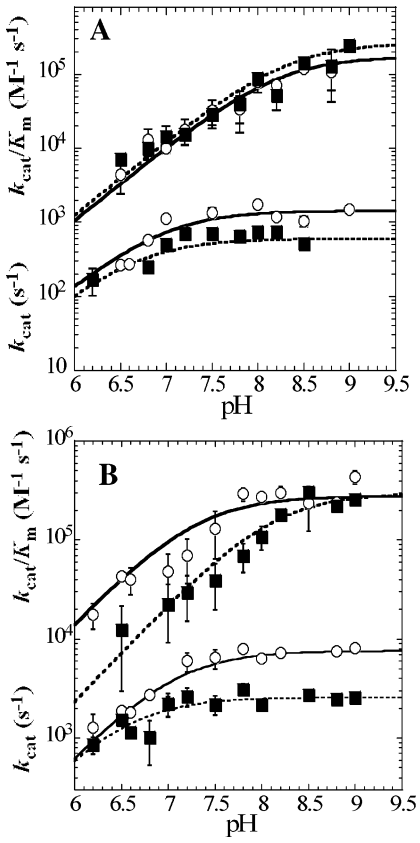

FIGURE 2: pH profiles of steady-state parameters for the Q75A and Q75N Cam variants. (A) Q75A (■) k_{cat}/K_m^{eff} of Co−Q75A and k_{cat}^{eff} of Co−Q75A and (○) k_{cat}/K_m^{eff} of Zn−Q75A and k_{cat}^{eff} of Zn−Q75A. (B) Q75N (■) k_{cat}/K_m^{eff} of Co−Q75N and k_{cat}^{eff} of Co−Q75N (○) k_{cat}/K_m^{eff} of Zn−Q75N and k_{cat}^{eff} of Zn−Q75N.

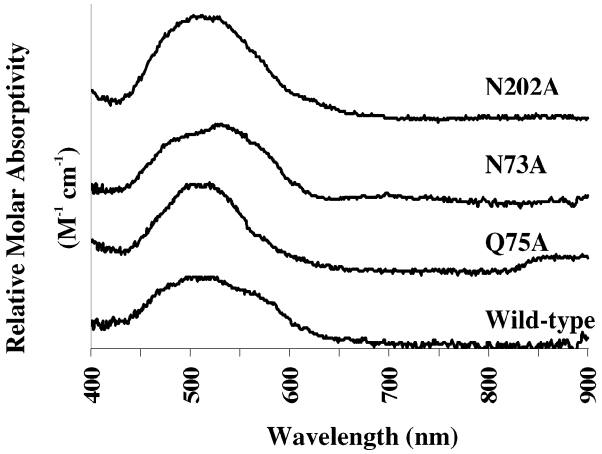

FIGURE 3: Optical absorption difference spectra of Co- *minus* Zn-substituted wild-type Cam and variants. Conditions were 1.1 mM Cam in 20 mM MOPS, pH 7.0, at 25 °C.

of the wild-type Co−Cam, indicating no major alteration of the metal environment. These spectroscopic data further support that changes made in the active site of the alanine variants did not interrupt the structural integrity of the active site.

Kinetic Analyses of Gln75 Variants. Residue Gln75 is positioned to act as a hydrogen bond acceptor to the attacking metal-bound hydroxide as inferred from the distance of the ϵO atom of Gln75 to the metal-bound oxygen of HCO_3^- in the wild-type Co−Cam structure (Figure 1). Steady-state kinetic parameters of Cam Gln75 variants are shown in Table 1. Conservative replacement of Gln75 with an Asn resulted in ~3% retention of the k_{cat}/K_m value in the Zn−Q75N variant and only 0.5% retention in the Co−Q75N variant when compared to the corresponding k_{cat}/K_m value of wild-type Cam. Similarly, the Q75A variants retained ~1% of the wild-type value (Table 1). Replacement of Gln75 with an Asp or Glu almost abolished the k_{cat}/K_m value relative to wild-type. These results support the proposed role for Gln75 in stabilizing and positioning the metal-bound hydroxide for attack on CO_2. It cannot be ruled out with certainty that conformational changes in the active site accounted for the decreases in k_{cat}/K_m. On the other hand, this explanation is less likely based on spectroscopic analysis of the Co−Q75A variant and that conservative replacement of Gln75 with Asn resulted in a maximum of only 3% retention of the k_{cat}/K_m value.

The proposed role of Gln75 was further examined by obtaining profiles of pH versus k_{cat} or k_{cat}/K_m of the Q75A and Q75N variants (Figure 2). Only the Q75N and Q75A variants exhibited enough observable activity to be assayed over a broad pH range. The steady-state parameter k_{cat}/K_m of the Q75N and Q75A variants was pH-dependent, although the profiles were best fit to a single pK_a (eq 4) compared to the two ionizations that were fit for wild-type Cam (Figure 2, Table 2), consistent with a previous report (*28*). The single pK_a (k_{cat}/K_m) values for all the variants were similar to the pK_a^{II} value of wild-type except for the Co−Q75N variant (Table 2). Both metal forms of the Q75N and Q75A variants had k_{cat}/K_m and k_{cat} values at pH 9.0 (Figure 2) that were less than 5% of the previously reported wild-type values (*28*) except for the Zn−Q75N k_{cat} value that was 13% of the wild-type (data not shown). These effects on k_{cat}/K_m for the Q75A and Q75N variants further support the proposed role for this residue in the CO_2 hydration step of catalysis. The kinetic parameter, k_{cat}, in wild-type Zn− and Co−Cam, was dependent on a single ionization within ~6.5−6.8 (Figure 2, Table 2).

Kinetic Analyses of Asn73 Variants. Discovery that Gln75 is essential for catalysis encouraged examination of the role of Asn73 which is ideally situated relative to Gln75 to provide a similar role as Glu106 in α-class CAs. As a secondary player in the proposed hydrogen bond network, the δO atom of Asn73 could potentially act as a hydrogen acceptor to the amide of Gln75 to orient Gln75 for hydrogen bonding with the catalytic metal-bound hydroxide (Figure 1). Steady-state kinetic parameters of Asn73 Cam variants are shown in Table 3. The Zn−N73A and Zn−N73Q variants yielded k_{cat}/K_m values that were ~40% of the corresponding zinc wild-type value, whereas Co−N73A, -Q and -D variants had ~20% of the k_{cat}/K_m values compared to wild-type Co−Cam. An exception to these results was the Zn−N73D variant which retained 100% of the wild-type Zn−Cam k_{cat}/K_m value. At pH 9.0, the Co−N73A and Zn−N73A variants had k_{cat}/K_m and k_{cat} values that were 7% and 10% of the respective wild-type values (data not shown). These data suggest that Asn73 is not essential for catalysis and is only important for optimal catalysis, possibly by orienting Gln75 for optimal interaction with the metal-bound hydroxide.

Kinetic Analyses of Asn202 Variants. The amide of Asn202 is within hydrogen bonding distance to a nonmetal-bound oxygen of the bicarbonate molecule in reported crystal structures (*8*) (Figure 1) and is similarly positioned to

Table 2: pH-Independent Michaelis−Menten Kinetic Parameters Obtained from the pH Dependence of CO_2 Hydration Catalyzed by Wild-Type Cam, Q75A Variant, and Q75N Variant

	wild-type		variant			
parameters[a]	Zn−Cam	Co−Cam	Zn−Q75N	Co−Q75N	Zn−Q75A	Co−Q75A
k_{cat} (ms^{-1})	61.2 ± 0.1	104.3 ± 0.2	7.6 ± 0.1	2.66 ± 0.03	1.5 ± 0.6	0.6 ± 0.01
pK_a (k_{cat})	6.8 ± 0.1	6.5 ± 0.1	7.0 ± 0.01	6.5 ± 0.06	6.9 ± 0.04	6.6 ± 0.01
pK_a^I (k_{cat}/K_m^I)	6.9 ± 0.1	6.7 ± 0.1	7.3 ± 0.04	8.1 ± 0.1	8.2 ± 0.08	8.3 ± 0.04
pK_a^{II} (k_{cat}/K_m^{II})	8.2 ± 0.3	8.4 ± 0.2	ND[b]	ND[b]	ND[b]	ND[b]
k_{cat}/K_m^I ($\mu M^{-1}\ s^{-1}$)	3.3 ± 0.5	5.3 ± 0.5	0.28 ± 0.01	0.30 ± 0.02	0.18 ± 0.02	0.28 ± 0.02
k_{cat}/K_m^{II} ($\mu M^{-1}\ s^{-1}$)	6.1 ± 0.5	15.1 ± 1.4	NA[b]	NA[b]	NA[b]	NA[b]

[a] pH-independent kinetic parameters and pK_a values for CO_2 hydration were determined by fitting pH-dependent k_{cat} and k_{cat}/K_m data obtained over the pH range of 6.2−9.0 to eq 4 as described in Experimental Procedures. [b] The kinetic parameter, k_{cat}/K_m, of these variants are dependent on a single pK_a, whereas in wild-type, k_{cat}/K_m is dependent on two pK_a's. ND, not detected; NA, not applicable.

Table 3: Michaelis-Menten Steady-State Kinetic Parameters for Wild-Type Cam and Variants with Substitutions at Asn73

variant	K_m (mM)	k_{cat}^{eff} (ms^{-1})[a]	k_{cat}/K_m^{eff} ($\mu M^{-1}\ s^{-1}$)[a]	molar ratio of metal/ monomer
wild-type Zn−Cam	15.6 ± 0.79	70.2 ± 7.8	4.35 ± 0.49	1.2
wild-type Co−Cam	15.3 ± 0.9	173.0 ± 4.5	11.7 ± 0.5	0.7
Zn−N73A	10.9 ± 0.09	20.1 ± 0.76	1.84 ± 0.086	1.0
Co−N73A	17.1 ± 0.25	56.8 ± 0.45	3.33 ± 0.07	0.7
Zn−N73Q	10.5 ± 1.1	19.7 ± 0.86	1.89 ± 0.28	1.0
Co−N73Q	13.9 ± 2.1	28.0 ± 2.04	2.00 ± 0.45	0.8
Zn−N73D	10.4 ± 0.7	44.5 ± 0.49	4.35 ± 0.34	0.8
Co−N73D	15.4 ± 1.4	45.5 ± 2.09	2.95 ± 0.41	1.0

[a] Effective k_{cat} and k_{cat}/K_m values were based on the concentration of monomer associated with an active site metal determined from the molar ratio of metal/monomer.

Table 4: Michaelis-Menten Steady-State Kinetic Parameters for Wild-Type Cam and Variants with Substitutions at Asn202

variant	K_m (mM)	k_{cat}^{eff} (ms^{-1})[a]	k_{cat}/K_m^{eff} ($\mu M^{-1}\ s^{-1}$)[a]	molar ratio of metal/ monomer
wild-type Zn−Cam	18.2 ± 0.79	76.3 ± 6.8	4.16 ± 1.1	1.0
wild-type Co−Cam	17.3 ± 0.9	173.0 ± 4.9	11.7 ± 0.50	0.7
Zn−N202A	26.2 ± 3.9	6.60 ± 0.60	0.25 ± 0.06	1.5
Co−N202A	24.6± 0.9	17.4 ± 0.40	0.71 ± 0.04	0.8
Zn−N202Q	18.4 ± 0.6	6.7 ± 1.4	0.36 ± 0.21	1.8
Co−N202Q	24.5 ± 1.8	2.60 ± 0.11	0.11 ± 0.0012	1.0
Zn−N202S	39.6 ± 5.4	5.1 ± 0.50	0.13 ± 0.03	2.0
Co−N202S	47.3 ± 5.0	12.3 ± 0.96	0.26 ± 0.0048	1.0
Zn−N202H	20.7 ± 14.4	2.78 ± 1.1	0.134 ± 0.145	1.4
Co−N202H	35.8 ± 12.9	15.6 ± 3.8	0.436 ± 0.2622	1.0
Zn−N202D	116.2 ± 6.6	9.74 ± 0.48	0.0838 ± 0.0088	1.0
Co−N202D	ND[b]	ND[b]	ND[b]	0.8
Zn−N202E	ND[b]	ND[b]	ND[b]	1.0
Co−N202E	ND[b]	ND[b]	ND[b]	0.7

[a] Effective k_{cat} and k_{cat}/K_m values were based on the concentration of monomer associated with an active site metal determined from the molar ratio of metal/monomer. [b] ND, not determinable. Kinetic analyses for these variants yielded rates near the limit of detection precluding reliable k_{cat} and k_{cat}/K_m values determined using the Michaelis−Menten equation.

function analogous to the backbone amide of α-class Thr199. The Zn−N202Q, Zn−N202A, and Co−N202A variants had k_{cat}/K_m values at pH 7.5 of 8.7%, 6.0%, and 6.1%, respectively, relative to the corresponding wild-type value at pH 7.5 (Table 4). The Co−N202Q, -S, -H and Zn−N202S and -H variants had k_{cat}/K_m values that were ~3% or less of wild-type values. The rates of CO_2 hydration for the Co−N202D, Zn−N202E, and Co−N202E variants were too low for a successful fit to the Michaelis−Menten equation (Table 4). The k_{cat} values for all Asn202 variants were equal to or less than 10% of wild-type k_{cat} values. Both metal forms of the Asn202 alanine variants had both k_{cat} and k_{cat}/K_m values at pH 9.0 that were less than or equal to 10% of the respective wild-type values at pH 9.0 (data not shown). The decreases in the kinetic constants of the Asn202 variants suggest Asn202 is important for catalysis and are consistent with the previously proposed role (*8*) in orienting and polarizing CO_2 for attack by the metal-bound hydroxide. Conformational changes in the active site potentially explain the decreases in k_{cat} and k_{cat}/K_m. However, spectroscopic analysis of the N202A variant and marked decreases in k_{cat} and k_{cat}/K_m for the conservative replacement of Asn202 with Gln suggest conformational changes did not contribute significantly to decreases in the kinetic constants.

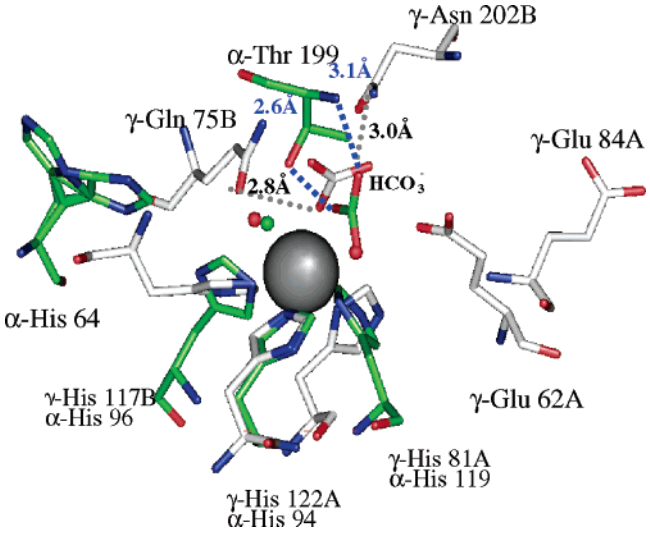

FIGURE 4: Co−Cam active site complexed with HCO_3^- superimposed with the Co−HCAII active site complexed with HCO_3^-. The figure was displayed with Open Source Pymol version 0.97 2004. Letters "A" and "B" designate residues contributed by adjacent monomers. The α or γ notation refers to residues belonging to α-class CA active site or γ-class CA active site. The HCAII active site members are represented in green, and the Cam active site members are represented in white. The smaller red spheres represent the coordinating waters of Co−Cam. The smaller green sphere depicts a conserved water in the Co−HCAII active site. Distances in blue refer to the distances from HCAII residues to HCAII bicarbonate. Distances in gray refer to the distances from Co−Cam residues to Co−Cam bicarbonate.

Superimposition of Cam Active Site and α-Class CA Active Site. The active site residues between the α-class CA

(HCAII) and the γ-class (Cam) bear no structural identity, except that the metal ligands superimpose (Figure 4). Also, the α-class CA bidentate-bound HCO_3^- shares approximately the same position with the bidentate-bound HCO_3^- in Co−Cam crystal structures (*8*). Remarkably, the ϵO atom of Gln75 and the hydroxyl of Thr199 are similarly situated relative to the respective metal-bound HCO_3^-, as is the amide of Asn202 and the backbone amide of Thr199. These comparative analyses further strengthen the proposed roles for Gln75 and Asn202 in Cam.

DISCUSSION

The crystal structures of three (α, β, and γ) of the six independently evolved classes of CAs reveal diversity in amino acid composition adjacent to the active site metal (*2*, *4*, *8*, *9*, *32*−*36*). However, these three classes have been kinetically described to participate in a two-step isomechanism involving a catalytic metal-bound hydroxide. This prompted investigations to determine if the γ-class, Cam, shares a common catalytic mechanism. Active site residues, Gln75 and Asn73, of the prototypic γ-class enzyme, Cam, are hypothesized to participate analogously to the α-class hydrogen bond network comprised of Zn−OH^-, Thr199, and Glu106 that aids in orienting the metal-bound hydroxide for attack on CO_2 (*8*, *11*, *13*, *27*). The Asn202 of Cam hypothetically polarizes the incoming CO_2 molecule, poising it for attack by the metal-bound hydroxide, akin to the function of the backbone amide of Thr199 (*8*). Here, we show that Gln75 and Asn202 are important for the CO_2 hydration step and propose a catalytic mechanism involving these residues.

Kinetic Analyses of Cam Variants Suggest Roles for Gln75, Asn202, and Asn73. The decreases in k_{cat}/K_m for the Zn− and Co−Q75A variants relative to wild-type indicate Gln75 is essential in the CO_2 hydration step of catalysis, consistent with a role in orienting the metal-bound hydroxide for attack on CO_2. Further, the Zn− and Co−Q75N variants retained less than 3% of the wild-type k_{cat}/K_m. Although the magnitude of decreases support an essential role for Gln75, decreases in k_{cat}/K_m for the α-class Thr199 variants were significantly less (*11*), which suggests a more stringent role for Thr199 that may be a consequence of differences in the active site architectures. The Gln75 variants also showed a similar decrease in k_{cat} when compared to wild-type Cam; thus, disruption of proton transfer cannot be ruled out. However, the functional group of Gln75 precludes a role for this residue in proton transfer, and therefore, it is unlikely that loss of proton transfer contributes significantly to the decrease in k_{cat}. Although retaining the potential to interact with the metal-bound hydroxide via the same functional group, the loss of one methylene group in the Q75N variants may not allow optimal hydrogen bonding with, or proper positioning of, the catalytic hydroxide. Interestingly, the carboxylate group of the Q75E variant, which could possibly act as a hydrogen bond acceptor, showed near abolition of k_{cat}/K_m. It is possible the glutamate has an electronegative charge that disorients the metal-bound hydroxide by repulsion, rearranges the active site, or both, impeding catalysis. This scenario may also explain the decreased k_{cat}/K_m value observed in the Q75D variants. Although gel filtration and spectroscopy of the Co−Q75A variant indicated no gross structural changes in the active site, it is possible that solvent rearrangement occurred in the Q75D variant that may have contributed to the observed reduction in catalysis.

In wild-type Zn− and Co−Cam, k_{cat}/K_m was dependent on two ionizable groups, one at ∼6.6−6.8 and a second at ∼8.0−8.3, which is in agreement with previous results (*7*). The first ionization (∼6.6−6.8) was previously assigned to the catalytic water (*7*), while it is unknown what group is responsible for the second pK_a. The pH profiles of k_{cat}/K_m for variants Q75A and Q75N showed a loss of the pK_a at ∼6.6−6.8, indicating Gln75 influences ionization of the catalytic water, a result consistent with the hypothesized function for Gln75 (*27*). It is reported that the pK_a of the catalytic water in the α-class CA (HCAII) increases at least 1 pH unit for Thr199 variants (*11*, *13*). Thus, one possible interpretation for the results is that Gln75 assists the metal in lowering the pK_a of the catalytic water by stabilization of the attacking hydroxide group relative to the water, and loss of the functional group in the Q75A variants results in an increased pK_a of the catalytic water that cannot be resolved from the pK_a at ∼8.3. The same explanation can be applied to interpret the profile of pH versus k_{cat}/K_m for the Co−Q75N variant, although the Zn−Q75N variant showed only a modest increase in the pK_a of the catalytic water and loss of the 8.3 pK_a which is unexplained. These results are consistent with the catalytic water within hydrogen bonding distance to Gln75 in both the Zn and Co enzymes which is also consistent with the proposed role for Gln75.

The kinetic parameter k_{cat} in wild-type Zn− and Co−Cam was dependent on a single ionization within ∼6.5−6.8. It is unknown what active site species may be responsible for this pK_a, although it was previously postulated to reflect the pK_a of a proton shuttle residue (*7*). The pH profiles of k_{cat} for the Q75A and Q75N variants showed retention of this pK_a, suggesting replacement of Gln75 does not influence the pK_a of the responsible residue.

The Asn73 variants showed only modest decreases in k_{cat} and k_{cat}/K_m relative to wild-type, whereas replacement of the α-class Glu106 with alanine or glutamine resulted in much larger decreases (*13*). Thus, if Asn73 functions in analogy to Glu106 in the α-class enzymes as previously proposed (*11*, *13*, *27*), then the requirement for a residue to orient Gln75 in Cam is less strict than for orienting Thr199 in the α-class and Asn73 has only a minor role in catalysis. This discrepancy may reflect differences in the active site architecture of Cam and the α-class CAs.

The decrease in k_{cat}/K_m for the Zn−N73D variant was not significantly different from the wild-type. One explanation for this result is that the carboxyl of N73D retains the ability to act as a hydrogen bond acceptor at essentially the same distance to Gln75 as in wild-type Cam. However, the decrease in k_{cat}/K_m of Co−N73D was comparable to that in other Co-substituted Asn73 variants. These discrepancies in k_{cat}/K_m between the Co- and Zn-substituted variants may involve the position of the metal-bound catalytic water adjacent to Gln75. Crystal structures reveal that the position of the water adjacent to Gln75 in Co−Cam is unique to that in Zn−Cam owing to the higher coordination of Co−Cam with three waters opposed to two waters for Zn−Cam (*8*). In the Zn−N73 variants, the hydrogen bonding between Gln75 and the catalytic hydroxide may remain intact, although not optimal for catalysis. In contrast, in the Co−N73D variant, the introduction of a negative charge may

Scheme 1: Proposed Mechanism for Cam[a]

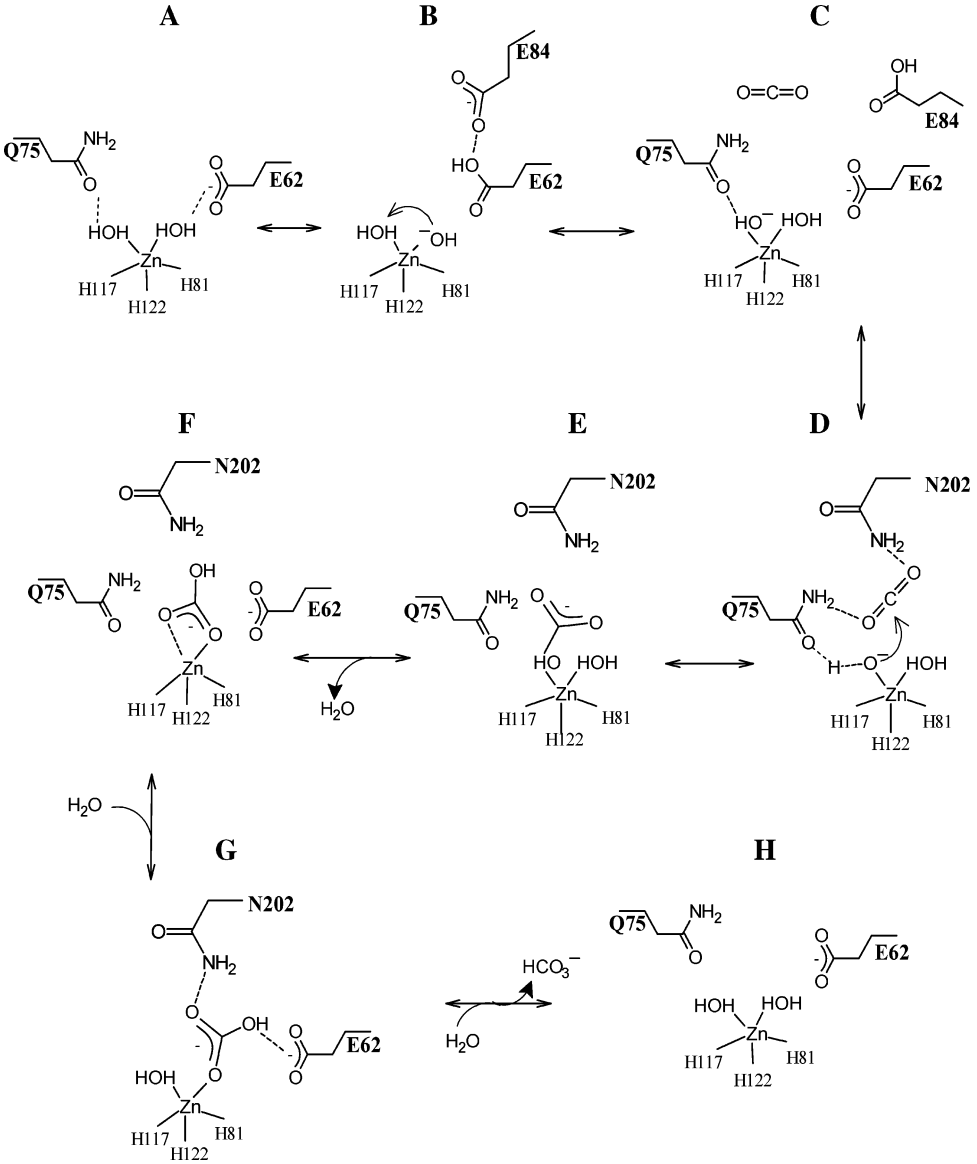

[a] The reaction mechanism is drawn using Zn−Cam as the template. Co−Cam is assumed to have a similar mechanism with an additional coordinating water molecule. (A) Zn^{2+} is coordinated by two water molecules. (B) Glu62, extracting a proton from a water, which then extracts a proton from the adjacent water. (C−F) The resulting Zn−OH^- attacks the CO_2 resulting in a bound HCO_3^- that displaces a water molecule. The HCO_3^- undergoes a bidentate transition state where the proton either rotates (Lindskog) or transfers (Lipscomb) to the nonmetal-bound oxygen of the HCO_3^-. (G) As shown in the crystal structures (*8*), Glu62 hydrogen-bonds with hydroxyl HCO_3^-, destabilizing it. An incoming water further destabilizes the HCO_3^- by replacing one of the bound oxygens. (H) A second incoming water completely displaces the HCO_3^- resulting in product removal and regeneration of the active site.

position Gln75 beyond favorable interactions with the catalytic hydroxide. Thus, the role of Asn73 may hold greater emphasis to properly angle and position Gln75 in higher coordinated metal centers.

Hakansson's proposal (*37*) that the backbone amide of Thr199 tethers the incoming CO_2 and destabilizes the HCO_3^- transition state has been substantiated by kinetic and structural data (*11*, *15*, *37*). In β-class CAs from *P. sativum* and *A. thaliana*, it has been suggested that Gln151 and Gln158 function comparable to the backbone amide of Thr199 (*15*, *37*). Cam crystal structures (*8*) reveal Asn202 is well-positioned to act analogous to these β-class residues as well as the backbone amide of Thr199 in α-class CAs. The 16-fold decrease in k_{cat}/K_m values for Asn202 variants relative to wild-type suggests that Asn202 is important for catalysis. Assuming no structural rearrangements were introduced, the $\Delta\Delta G^{\ddagger}$ ($-RT \ln[(k_{cat}/K_m^{variant})/(k_{cat}/K_m^{wild-type})]$) of the N202A variant estimates that the amide of Asn202 contributes ≅0.9 kcal/mol toward stabilization of the transition state. This contribution is comparable to the ≅0.8kcal/mol determined for the backbone amide of Thr199 (*11*). Thus, the kinetic analyses of the Asn202 variants are consistent with a role for this residue analogous to the backbone amide of Thr199 in the α-class CAs. Asn202 variants also showed large decreases in k_{cat} relative to wild-type. The functional group of Asn202 precludes a proton transfer function, and therefore, it is unlikely that loss of proton transfer contributes significantly to the decrease in k_{cat}.

Proposed Catalytic Mechanism of the Prototypic γ-Class Carbonic Anhydrase, Cam. Cumulating previous results and the results presented here, we propose a mechanism for the

prototypic γ-class CA, Cam (Scheme 1). Scheme 1 portrays Zn−Cam; however, the mechanism is also applicable to Co−Cam with the exception of an extra metal-coordinated water. Panel A shows Gln75 and Glu62 engaged in hydrogen bonds with separate waters, consistent with the crystal structure (*8*). A proton is extracted from the noncatalytic water coordinated by Glu62, sharing the proton between Glu62 and the previously documented (*26*) proton shuttle residue Glu84. The second pK_a in wild-type Cam at ~8.3 could reflect the ionization of the water within hydrogen bonding distance to Glu 62. Further experiments are needed to test this hypothesis. The metal-bound hydroxide then extracts a proton from the adjacent water hydrogen bonded by Gln75 (panel B). Now, the catalytic hydroxide hydrogen-bonded to Gln75 is primed for nucleophilic attack on the incoming CO_2 molecule, while the proton is relayed to Glu84 and ultimately shuttled out to buffer (panel C). The incoming CO_2 molecule is tethered by hydrogen bonds contributed by the functional group amides of Gln75 and Asn202 (panel D). The activated CO_2 is attacked by the lone pair of electrons of the metal-bound hydroxide, resulting in a metal-bound HCO_3^- (panel E). Then, the HCO_3^- swings down, binding in a bidentate fashion to the metal which displaces the coordinated water previously engaged in a hydrogen bond with Glu62 (panel F). Observed in structures of both Zn−Cam and Co−Cam, the bidentate-bound HCO_3^- displaces the same coordinating water (*8*). The proton of the hydroxyl of the bound HCO_3^- shifts (Lindskog transition state) to the oxygen tethered by Asn202 or the hydroxyl rotates via the carbon bond (Lipscomb transition state) as described for the α-class CA (*21*, *38*, *39*). An incoming water displaces an oxygen which results in monodentate-bound HCO_3^- supported via hydrogen bonds with Asn202 and Glu62 (panel G); however, roles for Gln75 and Asn202 in product removal are uncertain. Finally, a second water displaces the product from the active site (panel H).

This proposed catalytic mechanism portrays a more defined role for residue Glu62. A proton extraction and shuttle function was previously hypothesized based on crystal structures (*8*, *26*). Although previous kinetic analyses of variants indicate Glu62 as essential for the CO_2 hydration step (*26*), a more detailed function was not proposed. The mechanism proposed here suggests Glu62 is involved in product removal, contributing to the CO_2 hydration step and proton transfer. With the results presented here, it is not possible to deconvolute each contribution; however, structural (*8*, *26*) and kinetic analysis of variants (*8*, *26*) are reported that support involvement in both steps. A positive value for $\Delta\Delta G_B$ (k_{cat}) of the double E62A/E84A variant suggests these two residues act in an additive manner during the proton-transfer event (*26*). Further, Glu84 resides 8 Å from the metal-bound water (*8*), indicating an intervening residue or water is needed to relay the proton from the metal to buffer. Inspection of Cam crystal structures do not show conserved water(s) that may act as a relay; however, Glu62 is well-positioned in the active site to shuttle protons form the adjacent metal-bound water to Glu84. Indeed, in structures of Cam not complexed with HCO_3^-, Glu62 is in a shifted conformation sharing a proton with Glu84 (*8*).

Conclusions. This study has investigated roles for three active site residues (Gln75, Asn73, and Asn202) previously identified in crystal structures of the prototypic γ-class carbonic anhydrase (Cam). Kinetic analysis of variants revealed that Gln75 and Asn202 are important in catalysis and that Asn73 plays a supportive role. The study also provides a more complete catalytic mechanism constructed using the kinetic data presented here and previously reported structural analyses. This mechanism also suggests a possible role for residue Glu62 not previously proposed. As well, the investigation lends to the mounting evidence that, although the six classes of carbonic anhydrases evolved independently, at least three of these classes (α, β, and γ) utilize variations of a fundamental hydrogen bond network for catalysis.

ACKNOWLEDGMENT

We thank Dr. William Horracks for useful and thorough discussion of the spectral analysis of wild-type Cam and the Cam variants and Dr. Katsuhiko Murakami for his assistance in generating Figure 4. We also thank Dr. Chingkuang Tu, Dr. David Silverman, Marcy Hernick, and Dr. Carol Fierke for helpful suggestions and comments on this manuscript.

REFERENCES

1. Meldrum, N. N., and F. J. W. Roughton. (1933) Carbonic anhydrase. Its preparation and properties, *J. Physiol. 80*, 113−141.
2. Saito, R., Sato, T., Ikai, A., and Tanaka, N. (2004) Structure of bovine carbonic anhydrase II at 1.95 angstrom resolution, *Acta Crystallogr., Sect. D 60*, 792−795.
3. So, A. K. C., Espie, G. S., Williams, E. B., Shively, J. M., Heinhorst, S., and Cannon, G. C. (2004) A novel evolutionary lineage of carbonic anhydrase (epsilon class) is a component of the carboxysome shell, *J. Bacteriol. 186*, 623−630.
4. Strop, P., Smith, K. S., Iverson, T. M., Ferry, J. G., and Rees, D. C. (2001) Crystal structure of the "cab"-type beta class carbonic anhydrase from the archaeon *Methanobacterium thermoautotrophicum*, *J. Biol. Chem. 276*, 10299−10305.
5. Smith, K. S., Cosper, N. J., Stalhandske, C., Scott, R. A., and Ferry, J. G. (2000) Structural and kinetic characterization of an archaeal beta-class carbonic anhydrase, *J. Bacteriol. 182*, 6605−6613.
6. Cox, E. H., McLendon, G. L., Morel, F. M. M., Lane, T. W., Prince, R. C., Pickering, I. J., and George, G. N. (2000) The active site structure of *Thalassiosira weissflogii* carbonic anhydrase 1, *Biochemistry 39*, 12128−12130.
7. Alber, B. E., Colangelo, C. M., Dong, J., Stalhandske, C. M. V., Baird, T. T., Tu, C. K., Fierke, C. A., Silverman, D. N., Scott, R. A., and Ferry, J. G. (1999) Kinetic and spectroscopic characterization of the gamma-carbonic anhydrase from the methanoarchaeon *Methanosarcina thermophila*, *Biochemistry 38*, 13119−13128.
8. Iverson, T. M., Alber, B. E., Kisker, C., Ferry, J. G., and Rees, D. C. (2000) A closer look at the active site of γ-class carbonic anhydrases: High-resolution crystallographic studies of the carbonic anhydrase from *Methanosarcina thermophila*, *Biochemistry 39*, 9222−9231.
9. Kimber, M. S., and Pai, E. F. (2000) The active site architecture of *Pisum sativum* β-carbonic anhydrase is a mirror image of that of α-carbonic anhydrases, *EMBO J. 19*, 1407−1418.
10. Kogut, K. A., and Rowlett, R. S. (1987) A comparison of the mechanism of action of native and Co^{2+}-substituted carbonic anhydrase II, *J. Biol. Chem. 194*, 17.
11. Krebs, J. F., Ippolito, J. A., Christianson, D. W., and Fierke, C. A. (1993) Structural and functional importance of a conserved hydrogen-bond network in human carbonic anhydrase II, *J. Biol. Chem. 268*, 27458−27466.
12. Lesburg, C. A., and Christianson, D. W. (1995) X-ray crystallographic studies of engineered hydrogen-bond networks in a protein-zinc binding site, *J. Am. Chem. Soc. 117*, 6838−6844.
13. Liang, Z. W., Xue, Y. F., Behravan, G., Jonsson, B. H., and Lindskog, S. (1993) Importance of the conserved active-site residues Tyr7, Glu106 and Thr199 for the catalytic function of human carbonic anhydrase II, *Eur. J. Biochem. 211*, 821−827.
14. Rowlett, R. S., Chance, M. R., Wirt, M. D., Sidelinger, D. E., Royal, J. R., Woodroffe, M., Wang, Y. F. A., Saha, R. P., and

Lam, M. G. (1994) Kinetic and structural characterization of spinach carbonic-anhydrase, *Biochemistry 33*, 13967−13976.
15. Rowlett, R. S., Tu, C., Murray, P. S., and Chamberlin, J. E. (2004) Examination of the role of Gln-158 in the mechanism of CO_2 hydration catalyzed by beta-carbonic anhydrase from *Arabidopsis thaliana*, *Arch. Biochem. Biophys. 425*, 25−32.
16. Tripp, B. C., Bell, C. B., III, Cruz, F., Krebs, C., and Ferry, J. G. (2004) A role for iron in an ancient carbonic anhydrase, *J. Biol. Chem. 279*, 6683−6687.
17. Xue, Y. F., Liljas, A., Jonsson, B. H., and Lindskog, S. (1993) Structural-analysis of the zinc hydroxide-Thr199-Glu106 hydrogen-bond network in human carbonic anhydrase-II, *Proteins 17*, 93−106.
18. Silverman, D. N., and Lindskog, S. (1988) The catalytic mechanism of carbonic-anhydrase: Implications of a rate-limiting proteolysis of water, *Acc. Chem. Res. 21*, 30−36.
19. Silverman D. N., Vincent, S. H. (1984) Proton transfer in the catalytic mechanism of carbonic anhydrase, *CRC Crit. Rev. Biochem. 14*, 207−255.
20. Lindskog, S. (1997) Structure and mechanism of carbonic anhydrase, *Pharmacol. Ther. 74*, 1−20.
21. Bottoni, A., Lanza, C. Z., Miscione, G. P., and Spinelli, D. (2004) New model for a theoretical density functional theory investigation of the mechanism of the carbonic anhydrase: How does the internal bicarbonate rearrangement occur? *J. Am. Chem. Soc. 126*, 1542−1550.
22. Tautermann, C. S., Loferer, M. J., Voegele, A. F., and Liedl, K. R. (2003) About the kinetic feasibility of the Lipscomb mechanism in human carbonic anhydrase II, *J. Phys. Chem. B 107*, 12013−12020.
23. Krebs, J. F., and Fierke, C. A. (1993) Determinants of catalytic activity and stability of carbonic anhydrase II as revealed by random mutagenesis, *J. Biol. Chem. 268*, 948−954.
24. Campbell, I. D., and Raymond A. D. (1984) in *Biological Spectroscopy* (Elias, P., Ed.) pp 61−73, The Benjamin/Cummings Publishing Company, Inc., Menlo Park, CA
25. Alber, B. E., and Ferry, J. G. (1994) A carbonic-anhydrase from the archaeon *Methanosarcina thermophila*, *Proc. Natl. Acad. Sci. U.S.A. 91*, 6909−6913.
26. Tripp, B. C., and Ferry, J. G. (2000) A structure−function study of a proton transport pathway in the gamma-class carbonic anhydrase from *Methanosarcina thermophila*, *Biochemistry 39*, 9232−9240.
27. Merz, K. M. (1990) Insights into the function of the zinc hydroxide-Thr199-Glu106 hydrogen bonding network in carbonic anhydrases, *J. Mol. Biol. 214*, 799−802.
28. Alber, B. E., and Ferry, J. G. (1996) Characterization of heterologously produced carbonic anhydrase from *Methanosarcina thermophila*, *J. Bacteriol. 178*, 3270−3274.
29. Khalifah, R. G. (1971) The carbon dioxide hydration activity of carbonic anhydrase I. Stop-flow kinetic studies on the native human isoenzymes b and c, *J. Biol. Chem. 246*, 2561−2573.
30. Kim, Y. M., and Han, S. (2004) Peroxynitrite inactivates carbonic anhydrase II by releasing active site zinc ion, *Bull. Korean Chem. Soc. 25*, 711−714.
31. Mauksch, M., Brauer, M., Weston, J., and Anders, E. (2001) New insights into the mechanistic details of the carbonic anhydrase cycle as derived from the model system $(NH_3)_3ZnOH + CO_2$: How does the H_2O/HCO_3^- replacement step occur? *ChemBioChem 2*, 190−198.
32. Cronk J. D., Endrizzi, J. A., Cronk, M. R., O'Neill, J. W., and Zhang, K. Y. (2001) Crystal structure of *E. coli* beta-carbonic anhydrase, an enzyme with an unusual pH-dependent activity, *Protein Sci. 5*, 911−922.
33. Huang S., Xue, Y., Sauer-Eriksson, E., Chirica, L., Lindskog, S., and Jonsson B. H. (1998) Crystal structure of carbonic anhydrase from *Neisseria gonorrhoeae* and its complex with inhibitor acetozolamide, *J. Mol. Biol. 283*, 301−310.
34. Krebs, J. F., Rana, F., Dluhy, R. A., and Fierke C. A. (1993) Kinetic and spectroscopic studies of hydrophilic amino acid substitutions in the hydrophobic pocket of human carbonic anhydrase II, *Biochemistry 32*, 4496−4505.
35. Mitsuhashi, S, Mizushima, T., Yamashita, E., Yamamoto, M., Kumasaka, T., Moriyama, H., Ueki, T., Miyachi, S., and Tsukihara, T. (2000) X-ray structure of beta-carbonic anhydrase from the red alga, *Porphyridium* purpureum, reveals a novel catalytic site for CO_2 hydration, *J. Biol. Chem. 275*, 5521−5526.
36. Nair, S. K., and Christianson, D. (1993) Crystallographic studies of azide binding to human carbonic anhydrase II, *Eur. J. Biochem. 213*, 507−515.
37. Håkansson, K., Carlsson, M., Svensson, L. A., and Liljas, A. (1992) Structure of native and apo carbonic anhydrase II and structure of some of its anion-ligand complexes, *J. Mol. Biol. 227*, 4.
38. Lindskog, S., and Liljas, A. (1993) Carbonic anhydrase and the role of orientation in catalysis, *Curr. Opin. Struct. Biol. 3*, 915−920.
39. Thoms, S. (2002) Hydrogen bonds and the catalytic mechanism of human carbonic anhydrase II, *J. Theor. Biol. 215*, 399−404.

BI052507Y